

# A Semi-Implicit Method for Incompressible Three-Phase Flow in Porous Media\*

Justin Dong      Béatrice Rivière

## Abstract

In this paper, we present a semi-implicit method for the incompressible three-phase flow equations in two dimensions. In particular, a high order discontinuous Galerkin spatial discretization is coupled with a backward Euler discretization in time. We consider a pressure-saturation formulation, decouple the pressure and saturation equations and solve them sequentially while still keeping each equation implicit in its respective unknown. We present several numerical examples on both homogeneous and heterogeneous media, with varying permeability and porosity. Our results demonstrate the robustness of the scheme. In particular, no slope limiters are required and a relatively large time step may be taken.

## 1 Introduction

Many flow systems in porous media can be categorized as a three-phase flow, such as light oil, heavy oil, and water. Predicting the evolution of the phases in space and time is essential in the decision-making process for the oil and gas industry. The mathematical models are based on mass conservation laws for each phase. Two-phase flow models have been heavily studied in the literature and input functions such as capillary pressure and relative permeabilities are well-understood and validated by core-flooding experiments [8]. On one hand, three-phase flow models can be viewed as an extension of the two-phase flow models. On the other hand, there is less consensus on the appropriate choice of the capillary pressure and relative permeability curves and existing models from two-phase data may not agree with experimental results [3].

Our paper applies a discontinuous Galerkin (DG) method that uses piecewise polynomials of degree from one to four to solve the incompressible three-phase flow problem. DG methods have been successfully applied to single phase flow [5, 14] and to two-phase flow [16, 13, 15]. In particular, robustness of the methods for single-phase and two-phase flow in heterogeneous media was shown in [4, 17]. The lack of continuity between the mesh elements makes the DG method very suitable for flow and transport in porous media. Local mass conservation is an inherent property of the DG method. In addition, the method allows for discontinuous input data if discontinuity lines agree with the mesh skeleton. Any promising discretization of the three-phase flow problem should handle the strong heterogeneities of the medium. In this paper, we use realistic values for the permeability and porosity fields. We note that the permeability values usually vary across six orders of magnitude. These variations yield highly varying phase velocities via the generalized Darcy's law. Popular methods used by the oil and gas industry are the finite difference methods and the cell-centered finite volume methods. Both methods are only of first order and exhibit numerical diffusion, particularly in the case of heterogeneities [2, 18]. Other methods for solving the three-phase problem include mixed finite elements and streamline front tracking [9, 1, 7].

---

\*riviere@rice.edu; justin.dong@alumni.rice.edu; Both authors acknowledge the support of National Science Foundation grant NSF-DMS 1318348.

In a three-phase model, the unknowns, which are the saturation and pressure for each phase, are related through relations like capillary pressures. This results in three independent unknowns. In our work, we solve for the heavy oil pressure and the water and light oil saturations. We show convergence of the method for discontinuous input data, such as permeability and porosity fields. We vary the polynomial degree between one and four. This paper is related to a previous work for modeling three-phase flow in homogeneous one-dimensional domains [12]. In a recent paper, the DG method was applied to solve the black-oil problem in one-dimensional domains, which is a compressible three-phase flow. In addition, the gas phase is assumed to be miscible in the oil phase [20]. In [19], the finite volume method is combined with a DG method and slope limiters to solve the two-phase and three-phase flow problems in the absence of capillary pressure.

An outline of the paper follows. In the next section, we introduce the saturation and pressure equations and the input data. The numerical scheme is described in Section 4. Simulations on homogeneous and heterogeneous porous media are shown in Section 5. Conclusions follow.

## 2 The Model Problem

For a porous medium  $\Omega \subseteq \mathbb{R}^2$ , the incompressible three-phase flow formulation consists of a coupled system of three nonlinear partial differential equations. We denote the phases by liquid (heavy oil), aqueous (water), and vapor (light oil) and derive a pressure-saturation formulation using the pressure of the liquid phase. The pressure of the liquid phase is denoted by  $p_o$  and the saturations of the aqueous and vapor phases are denoted by  $s_w$  and  $s_g$ , respectively. We have:

$$\frac{\partial(\phi s_w)}{\partial t} + \nabla \cdot \left( \frac{\lambda_w}{\lambda_t} (\mathbf{u} + K \lambda_g p'_{cgo} \nabla s_w) - \nabla \cdot \left( K \frac{\lambda_w(\lambda_o + \lambda_g)}{\lambda_t} p'_{cwo} \nabla s_w \right) \right) = 0 \quad (1)$$

$$\frac{\partial(\phi s_g)}{\partial t} + \nabla \cdot \left( \frac{\lambda_g}{\lambda_t} (\mathbf{u} + K \lambda_w p'_{cwo} \nabla s_g) - \nabla \cdot \left( K \frac{\lambda_g(\lambda_o + \lambda_w)}{\lambda_t} p'_{cgo} \nabla s_g \right) \right) = 0 \quad (2)$$

and

$$\nabla \cdot \mathbf{u} = 0 \quad (3)$$

$$\mathbf{u} = -K \lambda_t \nabla p_o - K \lambda_w p'_{cwo} \nabla s_w - K \lambda_g p'_{cgo} \nabla s_g \quad (4)$$

Here,  $\mathbf{u}$  denotes the total velocity of the system. The porosity and permeability of the medium are denoted by  $\phi$  and  $K$ , respectively. The phase mobilities are denoted by  $\lambda_\alpha$  for  $\alpha \in \{w, o, g\}$  with the notion that the total mobility  $\lambda_t$  is given by  $\lambda_t = \lambda_w + \lambda_o + \lambda_g$ . The aqueous and vapor phase mobilities are functions of their respective saturations and viscosities, while the liquid phase mobility is a function of both the aqueous and vapor saturations and viscosities. In this paper, we take the following phase mobilities [21]:

$$\begin{aligned} \lambda_w(s_w) &= \frac{s_w^2}{\mu_w}, & \lambda_g(s_g) &= \frac{s_g^2}{\mu_g} \\ \lambda_o(s_w, s_g) &= \frac{(1 - s_w - s_g)(1 - s_w)(1 - s_g)}{\mu_o} \end{aligned} \quad (5)$$

The water-oil and gas-oil capillary pressures are denoted by  $p_{cwo}$  and  $p_{cgo}$ , respectively, and are defined as the difference in pressure of the respective phases:  $p_{cwo} = p_o - p_w$  and  $p_{cgo} = p_g - p_o$ . Using the notion that these capillary pressures are positive and decreasing, we see that  $p'_{cwo} < 0$  and  $p'_{cgo} < 0$ . We consider the following model of capillary pressures [6, 10]:

$$p_{cwo} = \frac{913.6890}{\ln \left( \frac{0.01}{1 - s_{wr}} \right)} \ln \left( \frac{s_w - s_{wr} + 0.01}{1 - s_{wr}} \right) \quad (6)$$

$$p_{\text{cgo}} = \frac{565.617}{\ln\left(\frac{0.01}{1 - s_{\text{wr}} - s_{\text{or}}}\right)} \ln\left(\frac{1.01 - s_{\text{g}} - s_{\text{wr}} - s_{\text{or}}}{1 - s_{\text{wr}} - s_{\text{or}}}\right) \quad (7)$$

Here, the residual saturations are denoted by  $s_{\alpha r}$ . For the boundary conditions, we partition  $\partial\Omega$  into several disjoint sets, namely:  $\partial\Omega = \Gamma_{p_1} \cup \Gamma_{p_2} = \Gamma_{s_1} \cup \Gamma_{s_2}$ . On the boundaries  $\Gamma_{p_1}$  and  $\Gamma_{s_1}$ , we have Dirichlet boundary conditions and on  $\Gamma_{p_2}$  and  $\Gamma_{s_2}$ , we have no-flow (zero Neumann) boundary conditions. For the pressure equation, we have:

$$p_o = p_{o,D}, \quad \text{on } \Gamma_{p_1} \quad (8)$$

$$K\lambda_t \nabla p_o = 0, \quad \text{on } \Gamma_{p_2} \quad (9)$$

For the saturation equations, we have:

$$s_w = s_{w,D}, \quad \text{on } \Gamma_{s_1} \quad (10)$$

$$K \frac{\lambda_w(\lambda_o + \lambda_g)}{\lambda_t} p'_{\text{cwo}} \nabla s_w \cdot \mathbf{n}_e = 0, \quad \text{on } \Gamma_{s_2} \quad (11)$$

and

$$s_g = s_{g,D}, \quad \text{on } \Gamma_{s_1} \quad (12)$$

$$K \frac{\lambda_g(\lambda_o + \lambda_w)}{\lambda_t} p'_{\text{cgo}} \nabla s_g \cdot \mathbf{n}_e = 0, \quad \text{on } \Gamma_{s_2} \quad (13)$$

### 3 Variational Formulation

We consider a partitioning  $\mathcal{M}_h$  of the computational domain  $\Omega$  into triangular elements. Furthermore, we denote the set of interior edges of  $\mathcal{M}_h$  by  $\Gamma_h^i$ . We define the subspace of discontinuous polynomial basis functions as

$$\mathcal{V} = \{v : v|_T \in \mathbb{P}_p(T), p \geq 1, T \in \mathcal{M}_h\}$$

Here,  $\mathbb{P}_p(T)$  denotes the space of all polynomials of degree  $p$  defined on the triangular element  $T$ .

For a given edge  $e \in \Gamma_h^i$ , we denote its element neighbors by  $T_1$  and  $T_2$  using the convention that  $T_1$  is the element with the lower global number. Furthermore, we define  $\mathbf{n}_e$  to be the unit normal vector that points from  $T_1$  to  $T_2$ . If  $e \in \partial\Omega$ , then we use the convention that  $\mathbf{n}_e$  points outward. For the DG variational formulation, we define the jump  $[ \cdot ]$  and average  $\langle \cdot \rangle$  of a function  $v$  along an edge  $e$ :

$$\begin{aligned} [v] &= v|_{T_1} - v|_{T_2} \\ \langle v \rangle &= \frac{1}{2}(v|_{T_1} + v|_{T_2}) \end{aligned}$$

#### 3.1 The Heavy Oil Pressure Equation

We first define the auxiliary variables  $\zeta = K\lambda_w p'_{\text{cwo}} \nabla s_w$  and  $\xi = K\lambda_g p'_{\text{cgo}} \nabla s_g$ . Then we can rewrite equations (3) and (4) as follows:

$$-\nabla \cdot (K\lambda_t \nabla p_o) = -\nabla \cdot \zeta - \nabla \cdot \xi \quad (14)$$

We multiply by a test function  $v \in \mathcal{V}$  and integrate by parts. Summing over all of the elements in  $\mathcal{M}_h$  and edges in  $\Gamma_h^i \cup \partial\Omega$ , we obtain:

$$\sum_{T \in \mathcal{M}_h} \int_T K\lambda_t \nabla p_o \cdot \nabla v - \sum_{e \in \Gamma_h^i \cup \Gamma_{p_1}} \int_e \langle K\lambda_t \nabla p_o \cdot \mathbf{n}_e \rangle [v] + \epsilon \sum_{e \in \Gamma_h^i \cup \Gamma_{p_1}} \int_e \langle K\lambda_t \nabla v \cdot \mathbf{n}_e \rangle [p_o]$$

$$\begin{aligned}
& + \sum_{e \in \Gamma_h^i \cup \Gamma_{p_1}} \frac{\sigma}{|e|} \int_e [p_o][v] = \sum_{T \in \mathcal{M}_h} \int_T \nabla v \cdot \zeta - \sum_{e \in \Gamma_h^i \cup \partial\Omega} \int_e \zeta^* \cdot \mathbf{n}_e[v] \\
& + \sum_{T \in \mathcal{M}_h} \int_T \nabla v \cdot \xi - \sum_{e \in \Gamma_h^i \cup \partial\Omega} \int_e \xi^* \cdot \mathbf{n}_e[v] + \sum_{e \in \Gamma_{p_1}} \int_e \left( \epsilon K \lambda_t \nabla v \cdot \mathbf{n}_e + \frac{\sigma}{|e|} v \right) p_{o,D}
\end{aligned} \tag{15}$$

Here,  $(\cdot)^*$  denotes the numerical upwind flux, defined on a given edge  $e \in \Gamma_h^i$  by:

$$\zeta^* = \begin{cases} \zeta|_{T_1}, & \langle \zeta \cdot \mathbf{n}_e \rangle \geq 0 \\ \zeta|_{T_2}, & \langle \zeta \cdot \mathbf{n}_e \rangle < 0 \end{cases} \quad \xi^* = \begin{cases} \xi|_{T_1}, & \langle \xi \cdot \mathbf{n}_e \rangle \geq 0 \\ \xi|_{T_2}, & \langle \xi \cdot \mathbf{n}_e \rangle < 0 \end{cases}$$

Additionally,  $\epsilon$  and  $\sigma$  are parameters that denote the variant of the DG method. For  $\epsilon = 1$  and  $\sigma \geq 0$ , we have the NIPG method. For  $\epsilon = -1$  and  $\sigma > 0$ , we have the SIPG method. Lastly,  $\epsilon = 0$  and  $\sigma > 0$  yields the IIPG method. We will allow these parameters to vary in our numerical simulations.

### 3.2 The Water Saturation Equation

We define the auxiliary variables  $\chi$  and  $\alpha$ :

$$\begin{aligned}
\chi(p_o, s_w, s_g) &= \mathbf{u}(p_o, s_w, s_g) + K \lambda_g p'_{cgo} \nabla s_g \\
\alpha(s_w, s_g) &= \frac{\lambda_w(\lambda_o + \lambda_g)}{\lambda_t} p'_{cwo}
\end{aligned}$$

and rewrite (1) as follows:

$$\frac{\partial(\phi s_w)}{\partial t} + \nabla \cdot \left( \frac{\lambda_w}{\lambda_t} \chi(p_o, s_w, s_g) \right) - \nabla \cdot (K \alpha(s_w, s_g) \nabla s_w) = 0 \tag{16}$$

We again multiply by a test function  $w \in \mathcal{V}$ , integrate by parts, and sum over the elements and edges to obtain:

$$\begin{aligned}
& \sum_{T \in \mathcal{M}_h} \int_T \frac{\partial(\phi s_w)}{\partial t} w + \sum_{T \in \mathcal{M}_h} \int_T K \alpha(s_w, s_g) \nabla s_w \cdot \nabla w - \sum_{e \in \Gamma_h^i \cup \Gamma_{s_1}} \int_e \langle K \alpha(s_w, s_g) \nabla s_w \cdot \mathbf{n}_e \rangle [w] \\
& + \epsilon \sum_{e \in \Gamma_h^i \cup \Gamma_{p_1}} \int_e \langle K \alpha(s_w, s_g) \nabla w \cdot \mathbf{n}_e \rangle [s_w] + \sum_{e \in \Gamma_h^i \cup \Gamma_{s_1}} \frac{\sigma}{|e|} \int_e [s_w][w] - \sum_{T \in \mathcal{M}_h} \int_T \nabla w \cdot \frac{\lambda_w}{\lambda_t} \chi(p_o, s_w, s_g) \\
& + \sum_{e \in \Gamma_h^i \cup \partial\Omega} \int_e \left( \frac{\lambda_w}{\lambda_t} \right)^* \chi(p_o, s_w, s_g) \cdot \mathbf{n}_e [w] = \sum_{e \in \Gamma_{s_1}} \int_e \left( \epsilon K \alpha(s_w, s_g) \nabla w \cdot \mathbf{n}_e + \frac{\sigma}{|e|} w \right) s_{w,D}
\end{aligned} \tag{17}$$

Here,  $(\lambda_w/\lambda_t)^*$  denotes the numerical upwind flux again.

### 3.3 The Light Oil Saturation Equation

We define the auxiliary variables  $\Lambda$  and  $\beta$ :

$$\begin{aligned}
\Lambda(p_o, s_w, s_g) &= \mathbf{u}(p_o, s_w, s_g) + K \lambda_w p'_{cwo} \nabla s_w \\
\beta(s_w, s_g) &= \frac{\lambda_g(\lambda_o + \lambda_w)}{\lambda_t} p'_{cgo}
\end{aligned}$$

and rewrite (2) as follows:

$$\frac{\partial(\phi s_g)}{\partial t} + \nabla \cdot \frac{\lambda_g}{\lambda_t} \mathbf{\Lambda}(p_o, s_w, s_g) - \nabla \cdot (K\beta(s_w, s_g)\nabla s_g) = 0 \quad (18)$$

We again multiply by a test function  $z \in \mathcal{V}$  and integrate by parts and sum over the elements and edges to obtain:

$$\begin{aligned} & \sum_{T \in \mathcal{M}_h} \int_T \frac{\partial(\phi s_g)}{\partial t} z + \sum_{T \in \mathcal{M}_h} \int_T K\beta(s_w, s_g)\nabla s_g \cdot \nabla z - \sum_{e \in \Gamma_h^i \cup \Gamma_{s_1}} \int_e \langle K\beta(s_w, s_g)\nabla s_g \cdot \mathbf{n}_e \rangle [z] \\ & + \epsilon \sum_{e \in \Gamma_h^i \cup \Gamma_{p_1}} \int_e \langle K\beta(s_w, s_g)\nabla z \cdot \mathbf{n}_e \rangle [s_g] + \sum_{e \in \Gamma_h^i \cup \Gamma_{s_1}} \frac{\sigma}{|e|} \int_e [s_g][z] - \sum_{T \in \mathcal{M}_h} \int_T \nabla w \cdot \frac{\lambda_g}{\lambda_t} \mathbf{\Lambda}(p_o, s_w, s_g) \\ & + \sum_{e \in \Gamma_h^i \cup \partial\Omega} \int_e \left( \frac{\lambda_g}{\lambda_t} \right)^* \mathbf{\Lambda}(p_o, s_w, s_g) \cdot \mathbf{n}_e [z] = \sum_{e \in \Gamma_{s_1}} \int_e \left( \epsilon K\beta(s_w, s_g)\nabla z \cdot \mathbf{n}_e + \frac{\sigma}{|e|} z \right) s_{g,D} \end{aligned} \quad (19)$$

Here,  $(\lambda_g/\lambda_t)^*$  denotes the numerical upwind flux again.

## 4 Fully Discrete Scheme

For the saturation equations, we discretize the transient term using the backward Euler method. We denote the solutions at the  $k^{th}$  time step by  $(p_o^k, s_w^k, s_g^k)$ . The solutions at time  $t = 0$  are denoted by  $s_w^0, s_g^0$  and computed using  $L^2$  projections on the initial conditions.

For the oil pressure equation, we time lag the saturations, effectively linearizing the source terms and diffusion coefficients. For the water saturation equation, we time lag the coefficients using the values of the heavy oil pressure and light oil saturations, but the equation is kept nonlinear with respect to the water saturation equation. Similarly, the light oil saturation is kept nonlinear with respect to the light oil saturation unknown, while using the computed values for the oil pressure and water saturation from the previous steps. At each time step, we resolve the nonlinearity using Newton's method. Given  $(p_o^k, s_w^k, s_g^k) \in \mathcal{V} \times \mathcal{V} \times \mathcal{V}$ , we seek  $(p_o^{k+1}, s_w^{k+1}, s_g^{k+1}) \in \mathcal{V} \times \mathcal{V} \times \mathcal{V}$  such that for all  $(v, w, z) \in \mathcal{V} \times \mathcal{V} \times \mathcal{V}$ , we have:

$$\begin{aligned} & \sum_{T \in \mathcal{M}_h} \int_T K\lambda_t(s_w^k, s_g^k)\nabla p_o^{k+1} \cdot \nabla v - \sum_{e \in \Gamma_h^i \cup \Gamma_{p_1}} \int_e \langle K\lambda_t(s_w^k, s_g^k)\nabla p_o^{k+1} \cdot \mathbf{n}_e \rangle [v] + \\ & \epsilon \sum_{e \in \Gamma_h^i \cup \Gamma_{p_1}} \int_e \langle K\lambda_t(s_w^k, s_g^k)\nabla v \cdot \mathbf{n}_e \rangle [p_o^{k+1}] + \sum_{e \in \Gamma_h^i \cup \Gamma_{p_1}} \frac{\sigma}{|e|} \int_e [p_o^{k+1}][v] = \sum_{T \in \mathcal{M}_h} \int_T \nabla v \cdot \zeta^k - \\ & \sum_{e \in \Gamma_h^i \cup \partial\Omega} \int_e (\zeta^k)^* \cdot \mathbf{n}_e [v] - \sum_{T \in \mathcal{M}_h} \int_T \nabla v \cdot \xi^k - \sum_{e \in \Gamma_h^i \cup \partial\Omega} \int_e (\xi^k)^* \cdot \mathbf{n}_e [v] + \\ & \sum_{e \in \Gamma_{p_1}} \int_e \left( \epsilon K\lambda_t(s_w^k, s_g^k)\nabla v \cdot \mathbf{n}_e + \frac{\sigma}{|e|} v \right) p_{o,D} \end{aligned} \quad (20)$$

and

$$\begin{aligned} & \sum_{T \in \mathcal{M}_h} \frac{1}{\Delta t} \int_T \phi s_w^{k+1} w + \sum_{T \in \mathcal{M}_h} \int_T K\alpha(s_w^{k+1}, s_g^k)\nabla s_w^{k+1} \cdot \nabla w + \\ & \sum_{e \in \Gamma_h^i \cup \Gamma_{s_1}} \int_e \langle K\alpha(s_w^{k+1}, s_g^k)\nabla s_w^{k+1} \cdot \mathbf{n}_e \rangle [w] + \epsilon \sum_{e \in \Gamma_h^i \cup \Gamma_{s_1}} \int_e \langle K\alpha(s_w^{k+1}, s_g^k)\nabla w \cdot \mathbf{n}_e \rangle [s_w^{k+1}] + \end{aligned}$$

$$\begin{aligned}
& \sum_{e \in \Gamma_h^i \cup \Gamma_{s_1}} \frac{\sigma}{|e|} \int_e [s_w^{k+1}] [w] - \sum_{T \in \mathcal{M}_h} \int_T \nabla w \cdot \frac{\lambda_w(s_w^{k+1})}{\lambda_t(s_w^{k+1}, s_g^k)} \chi(p_o^{k+1}, s_w^k, s_g^k) + \\
& \sum_{e \in \Gamma_h^i \cup \partial\Omega} \int_e \left( \frac{\lambda_w(s_w^{k+1})}{\lambda_t(s_w^{k+1}, s_g^k)} \right)^* \langle \chi(p_o^{k+1}, s_w^k, s_g^k) \cdot \mathbf{n}_e \rangle [w] = \sum_{T \in \mathcal{M}_h} \frac{1}{\Delta t} \int_T \phi s_w^k w \\
& + \sum_{e \in \Gamma_{s_1}} \int_e \left( \epsilon K \alpha(s_w^{k+1}, s_g^k) \nabla w \cdot \mathbf{n}_e + \frac{\sigma}{|e|} v \right) s_{w,D}
\end{aligned} \tag{21}$$

and

$$\begin{aligned}
& \sum_{T \in \mathcal{M}_h} \frac{1}{\Delta t} \int_T \phi s_g^{k+1} z + \sum_{T \in \mathcal{M}_h} \int_T K \beta(s_w^{k+1}, s_g^{k+1}) \nabla s_g^{k+1} \cdot \nabla z + \\
& \sum_{e \in \Gamma_h^i \cup \Gamma_{s_1}} \int_e \langle K \beta(s_w^{k+1}, s_g^{k+1}) \nabla s_g^{k+1} \cdot \mathbf{n}_e \rangle [z] + \sum_{e \in \Gamma_h^i \cup \Gamma_{s_1}} \int_e \langle K \beta(s_w^{k+1}, s_g^{k+1}) \nabla z \cdot \mathbf{n}_e \rangle [s_g^{k+1}] + \\
& \sum_{e \in \Gamma_h^i \cup \Gamma_{s_1}} \frac{\sigma}{|e|} \int_e [s_g^{k+1}] [z] - \sum_{T \in \mathcal{M}_h} \int_T \nabla z \cdot \frac{\lambda_g(s_g^{k+1})}{\lambda_t(s_w^{k+1}, s_g^{k+1})} \Lambda(p_o^{k+1}, s_w^{k+1}, s_g^k) + \\
& \sum_{e \in \Gamma_h^i \cup \partial\Omega} \int_e \left( \frac{\lambda_g(s_g^{k+1})}{\lambda_t(s_w^{k+1}, s_g^k)} \right)^* \langle \Lambda(p_o^{k+1}, s_w^{k+1}, s_g^k) \cdot \mathbf{n}_e \rangle [z] = \sum_{T \in \mathcal{M}_h} \frac{1}{\Delta t} \int_T \phi s_g^k z \\
& + \sum_{e \in \Gamma_{s_1}} \int_e \left( \epsilon K \beta(s_w^{k+1}, s_g^{k+1}) \nabla z \cdot \mathbf{n}_e + \frac{\sigma}{|e|} v \right) s_{g,D}
\end{aligned} \tag{22}$$

## 5 Numerical Results

### 5.1 Homogeneous Medium

For the first numerical simulation, we consider a square kilometer computational domain  $\Omega = [0 \text{ m}, 1000 \text{ m}]^2$ . We take the residual saturations  $s_{wr} = 0$  and  $s_{or} = 0$ . We take the following viscosities:

$$\mu_w = 0.0001 \frac{\text{kg}}{\text{m} \cdot \text{s}} \quad \mu_o = 0.0005 \frac{\text{kg}}{\text{m} \cdot \text{s}} \quad \mu_g = 0.00001 \frac{\text{kg}}{\text{m} \cdot \text{s}}$$

We consider a uniform mesh of 2048 triangular elements with  $K = 10^{-10} \text{ m}^2$  and  $\phi = 0.2$  for all  $(x, y) \in \Omega$ . We define the left and right boundaries to be the Dirichlet boundaries as follows:

$$\begin{aligned}
p_o(x = 0 \text{ m}) &= 19.0 \text{ MPa} & p_o(x = 1000 \text{ m}) &= 15.0 \text{ MPa} \\
s_w(x = 0 \text{ m}) &= 0.82 & s_w(x = 1000 \text{ m}) &= 0.30 \\
s_g(x = 0 \text{ m}) &= 0.11 & s_g(x = 1000 \text{ m}) &= 0.54
\end{aligned}$$

We first use the NIPG method with  $\sigma = 1.0$ . We take  $p \in \{1, 2, 3, 4\}$  and a time step of  $\Delta t = 0.1$  days. The saturation profiles after 100 days are given in Figure 1.

We see that quadratic basis functions offer a significant increase in accuracy over linear basis functions. Cubic and quartic basis functions offer a further, but less noticeable increase in accuracy.

### 5.2 Inhomogeneous Medium

For the second numerical simulation, we use the same parameters as in the first simulation but imbed a large impermeable region  $\Omega_K \subseteq \Omega$  where  $K = 10^{-13} \text{ m}^2$ . We take  $\Omega_K = [250 \text{ m}, 750 \text{ m}]^2$ .

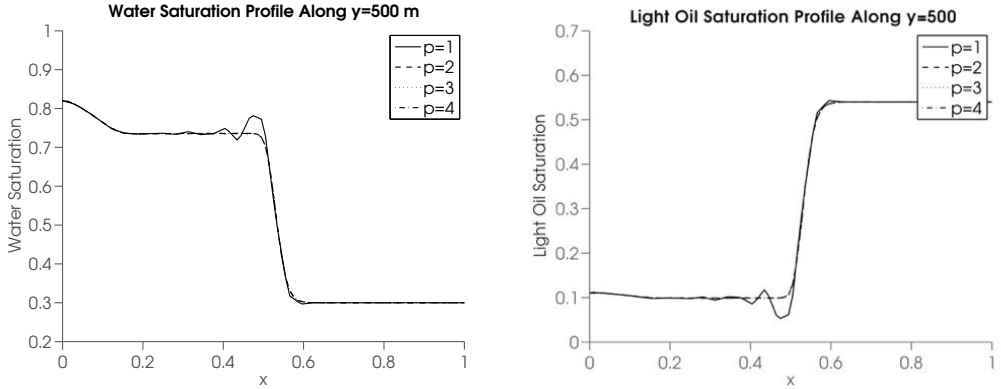


Figure 1: A comparison of the saturation profiles for  $p \in \{1, 2, 3, 4\}$  after 100 days.

We consider a mesh of 9800 triangular elements that is refined greatly in a small region around  $\partial\Omega_K$  as shown in Figure 2. We use the NIPG method with  $\sigma = 1.0$ . We take a time step of  $\Delta t = 0.1$  days. The two-dimensional pressure and saturation contours at 113 and 226 days are given in Figures 3 and 4 for the piecewise quadratic approximations ( $p = 2$ ). The pressure and saturation profiles along the line  $y = 500$  m are given in Figures 5 and 6.

We see that the scheme is able to accurately capture the impermeable regions. Furthermore, the solution at the boundary of  $\Omega_K$  remains sharp and well-pronounced; there is very little overshoot and undershoot and no slope limiters are required. The semi-implicit scheme allows us to take a relatively large time step and still obtain a stable solution. Newton's method always converges within 2 to 3 iterations using a tolerance of  $10^{-11}$  for this example.

Next, we consider varying the degree of the polynomial basis functions. We take  $\sigma = 1.0$ ,  $\Delta t = 1.0$  days, and  $p \in \{1, 2, 3\}$ . The saturation profiles along the midline  $y = 500$  m after 110 days are given in Figure 7. The saturation profiles along the upper edge of the domain after 110 days are given in Figure 8. We see that although each basis is able to effectively capture the behavior of the region of lower permeability in the center of the domain, the behavior in the vicinity of  $\partial\Omega$  varies considerably. For  $p = 1$ , spurious oscillations and significant overshoot and undershoot can be seen. As we increase the order of the basis to  $p = 2, 3$ , we see a much smoother solution.

### 5.3 Convergence Study

We test the numerical convergence of the scheme by (1) varying the mesh size and (2) varying the degree of the polynomial basis functions. We consider a  $120 \times 54$  cell cut of the 30th vertical layer of the permeability field from the data in [11]. We fix the porosity to be 0.20 throughout the domain. We first consider the effect of  $h$ -refinement on the solution. We consider three partitions of the computational domain  $\Omega = [0 \text{ m}, 1000 \text{ m}] \times [0 \text{ m}, 500 \text{ m}]$ :  $\mathcal{M}_1$ ,  $\mathcal{M}_2$ , and  $\mathcal{M}_3$  consisting of 4,096, 16,384, and 65,536 uniform triangular elements, respectively. The permeability field is upscaled to adhere to the coarsest mesh,  $\mathcal{M}_1$ , as shown in Figure 9. The permeability varies over six orders of magnitude.

The two-dimensional pressure and saturation contours after 65 days are given in Figures 10-12. The one-dimensional saturation profiles along  $y = 100$  m are given in Figure 13. We see that there is relatively little variance among the solutions on each mesh.

Next, we consider the effect of  $p$ -refinement on the solution. Namely, we fix the mesh to contain 16,384 uniform triangular elements as in  $\mathcal{M}_2$  and take  $p \in \{1, 2, 3\}$ .

The two-dimensional pressure and saturation contours after 65 days are given in Figures 14-16. The one-dimensional saturation profiles along  $y = 100$  m are given in Figure 17. We see again that

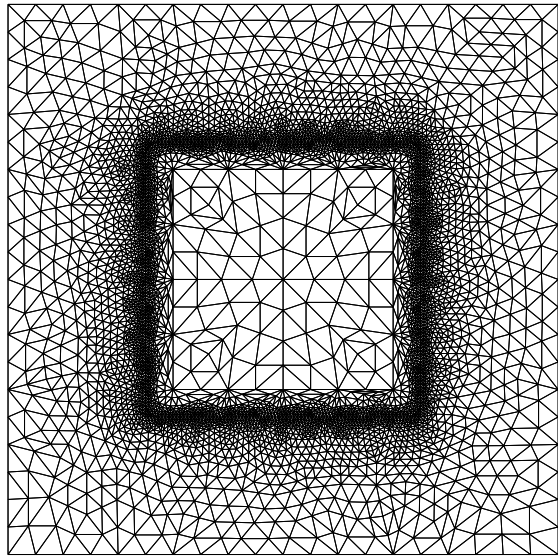


Figure 2: The refined mesh for the second example of a inhomogeneous medium with  $\Omega_K = [250 \text{ m}, 750 \text{ m}]^2$ .

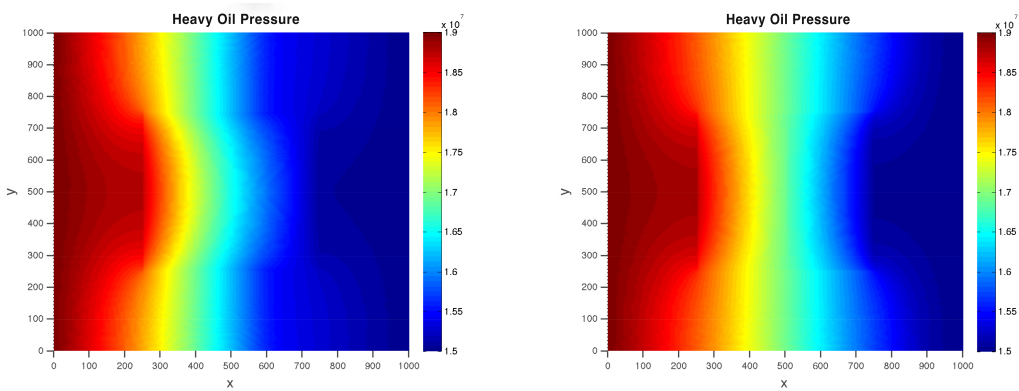


Figure 3: The two-dimensional pressure contours at 113 (left) and 226 (right) days for the example on an inhomogeneous medium using NIPG with  $\sigma = 1.0$  and  $p = 2$ .

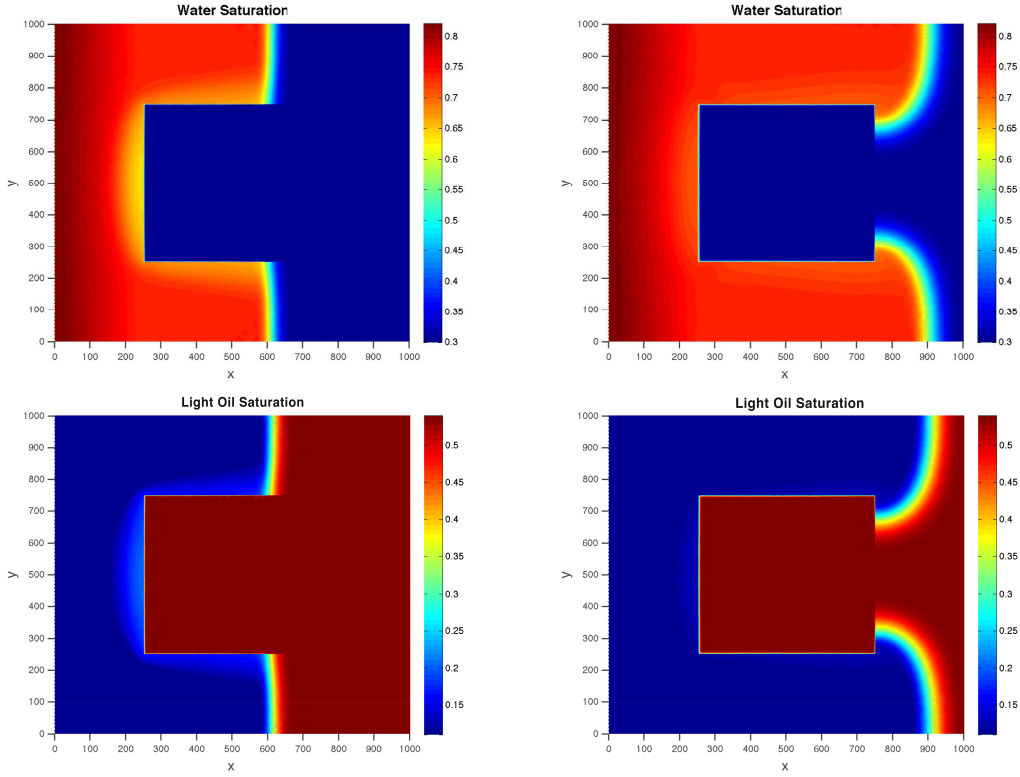


Figure 4: The two-dimensional saturation contours at 113 (left) and 226 (right) days for the example on an inhomogeneous medium using NIPG with  $\sigma = 1.0$  and  $p = 2$ .

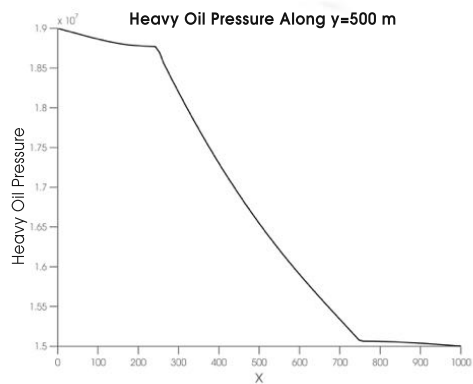


Figure 5: The pressure profile along  $y = 500$  at 113 days for the example on an inhomogeneous medium using NIPG with  $\sigma = 1.0$  and  $p = 2$ .

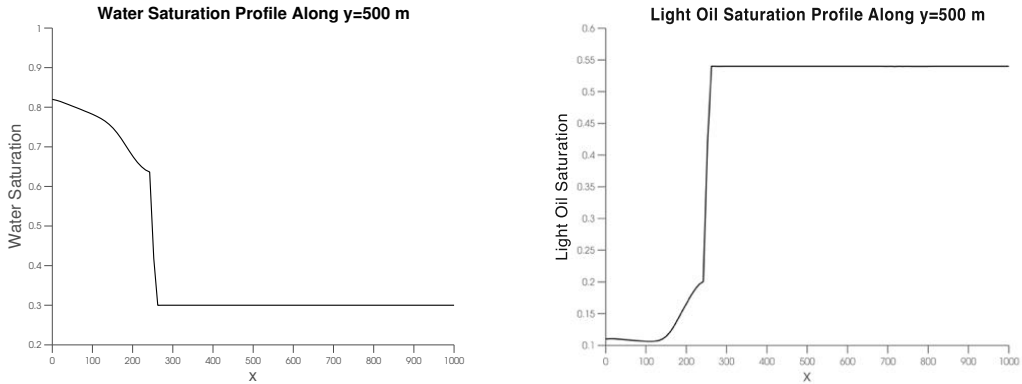


Figure 6: The saturation profiles along  $y = 500$  at 113 days for the example on an inhomogeneous medium using NIPG with  $\sigma = 1.0$  and  $p = 2$ .

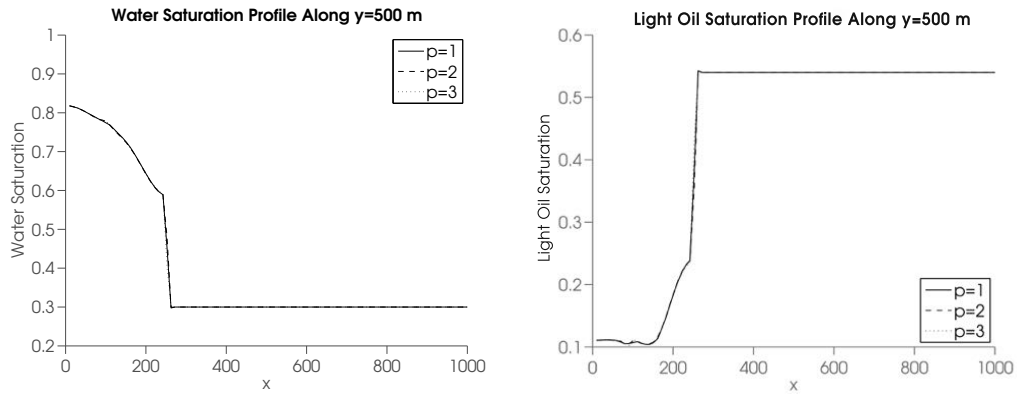


Figure 7: A comparison of the saturation profiles along  $y = 500$  m for  $p \in \{1, 2, 3\}$  after 110 days.

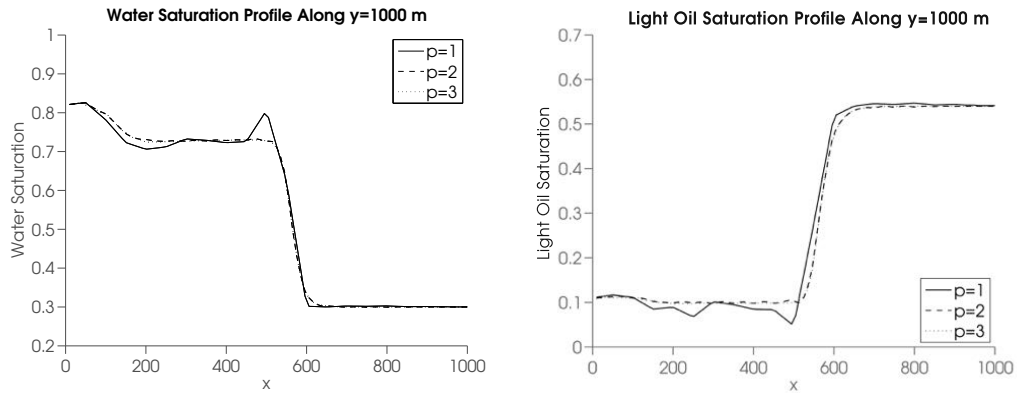


Figure 8: A comparison of the saturation profiles along  $y = 1000$  m for  $p \in \{1, 2, 3\}$  after 110 days.

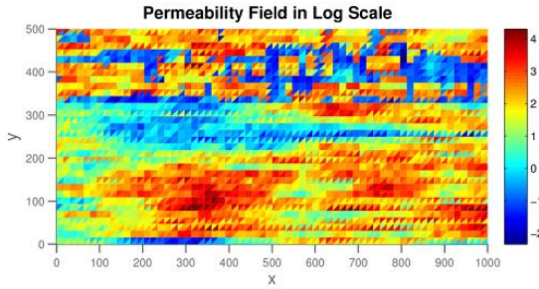


Figure 9: The permeability field corresponding to  $\mathcal{M}_1$  for the  $h$ -convergence study.

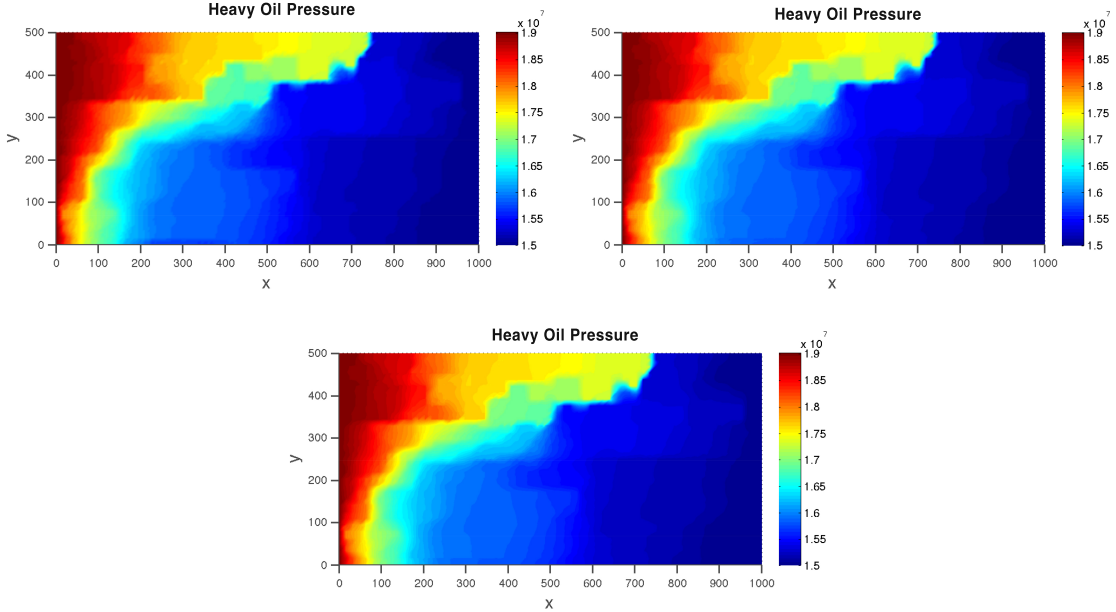


Figure 10: The two-dimensional pressure contours at 65 days for the convergence study example on  $\mathcal{M}_1$  (top),  $\mathcal{M}_2$  (middle), and  $\mathcal{M}_3$  (bottom) using NIPG with  $\sigma = 1.0$  and  $p = 2$ .

there is relatively little variance among the solutions. However, it should be noted that the solution for  $p = 1$  varies more than between  $p = 2$  and  $p = 3$ .

Lastly, we consider the same problem on  $\mathcal{M}_2$  with  $p = 2$ . We compare the solutions using NIPG and SIPG with  $\sigma = 1.0$  after 65 days. The saturation profiles are given in Figure 18. We see that there is little difference between the solutions regardless of the variant of DG method that is used.

#### 5.4 Local Mass Conservation

We now consider the local mass balance in our numerical scheme. The mass loss for the phase saturations on element  $T$  at the  $k^{th}$  time step are given by:

$$E_{s_o, T}^k = \frac{1}{\Delta t} \int_T \phi (s_o^k - s_o^{k-1}) + \int_{\partial T} \{\mathbf{u}_o^k \cdot \mathbf{n}_e\} \quad (23)$$

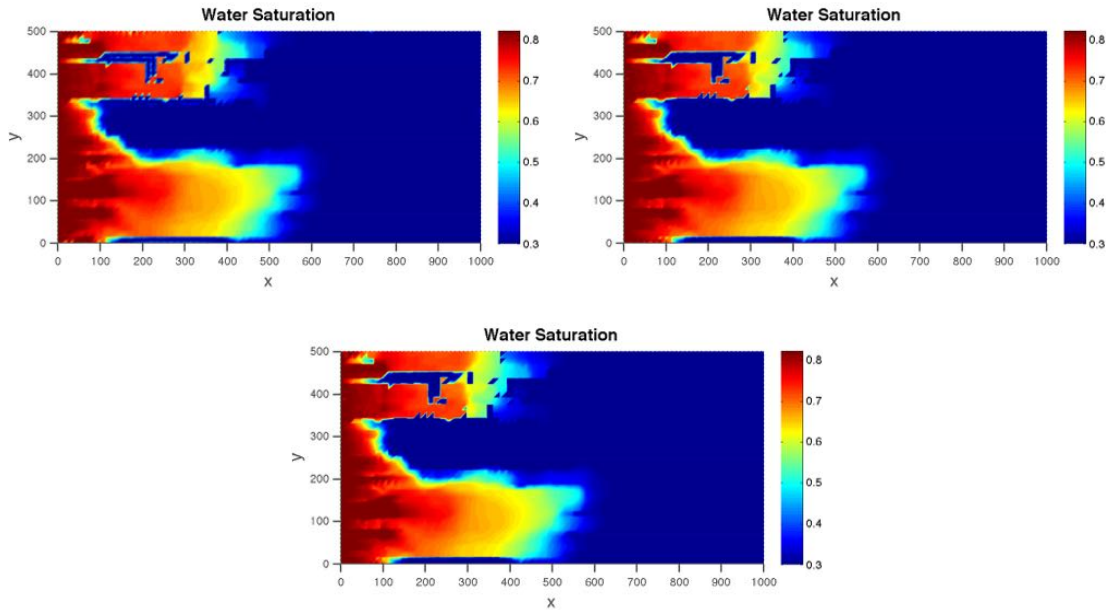


Figure 11: The two-dimensional water saturation contours at 65 days for the convergence study example on  $\mathcal{M}_1$  (top),  $\mathcal{M}_2$  (middle), and  $\mathcal{M}_3$  (bottom) using NIPG with  $\sigma = 1.0$  and  $p = 2$ .

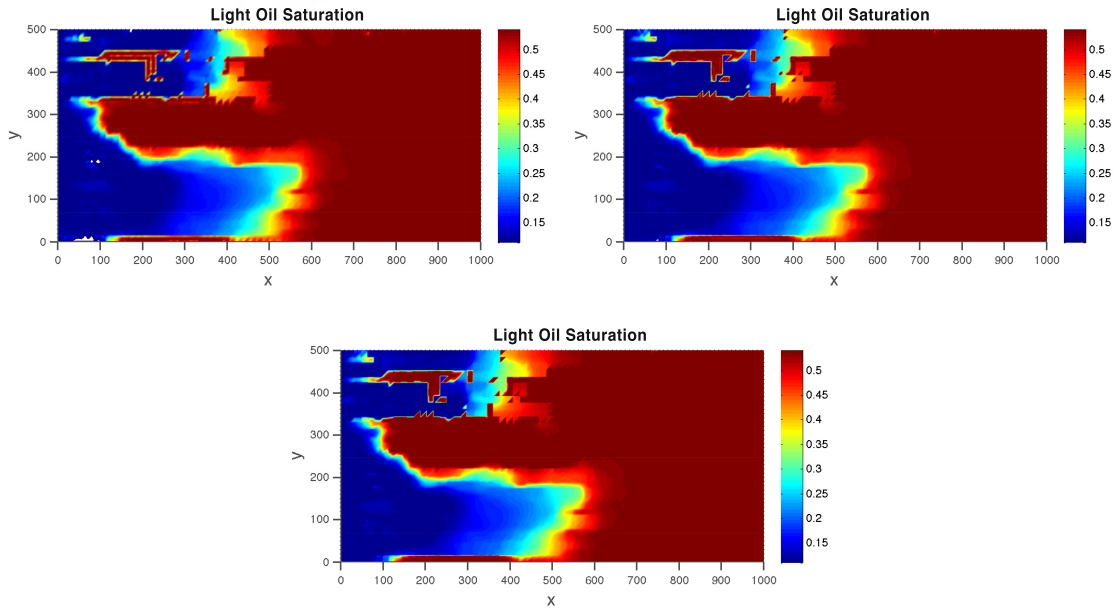


Figure 12: The two-dimensional light oil saturation contours at 65 days for the convergence study example on  $\mathcal{M}_1$  (top),  $\mathcal{M}_2$  (middle), and  $\mathcal{M}_3$  (bottom) using NIPG with  $\sigma = 1.0$  and  $p = 2$ .

$$E_{s_w, T}^k = \frac{1}{\Delta t} \int_T \phi (s_w^k - s_w^{k-1}) + \int_{\partial T} \{ \mathbf{u}_w^k \cdot \mathbf{n}_e \} \quad (24)$$

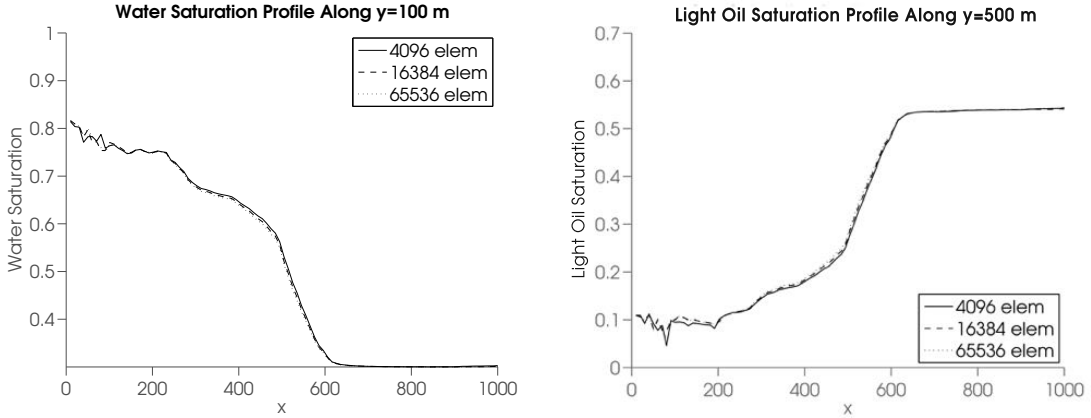


Figure 13: The one-dimensional saturation contours at 65 days for the convergence study example on  $\mathcal{M}_1$  (solid line),  $\mathcal{M}_2$  (dashed line), and  $\mathcal{M}_3$  (dotted line) using NIPG with  $\sigma = 1.0$  and  $p = 2$ .

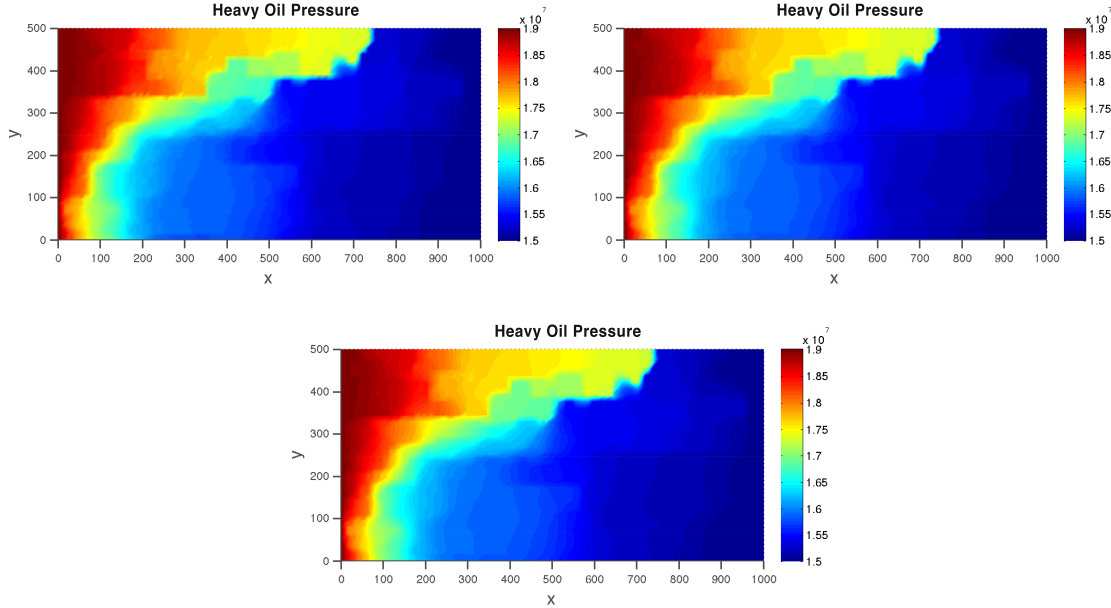


Figure 14: The two-dimensional pressure contours at 65 days for the convergence study example on  $\mathcal{M}_2$  using NIPG with  $p = 1$  (top),  $p = 2$  (middle), and  $p = 3$  (bottom) and  $\sigma = 1.0$ .

$$E_{s_g, T}^k = \frac{1}{\Delta t} \int_T \phi (s_g^k - s_g^{k-1}) + \int_{\partial T} \{\mathbf{u}_g^k \cdot \mathbf{n}_e\} \quad (25)$$

where the individual phase velocities are given by:

$$\mathbf{u}_o^k = -K\lambda_o(s_w^k, s_g^k)\nabla p_o^k \quad (26)$$

$$\mathbf{u}_w^k = -K\lambda_w(s_w^k)(\nabla p_o^k - p'_{cwo}(s_w^k)\nabla s_w^k) \quad (27)$$

$$\mathbf{u}_g^k = -K\lambda_g(s_g^k)(\nabla p_o^k - p'_{cgo}(s_g^k)\nabla s_g^k) \quad (28)$$

We compute the mass loss for the simulations given in Section 5.3 for the choice of  $\Delta t = 1.0$  day.

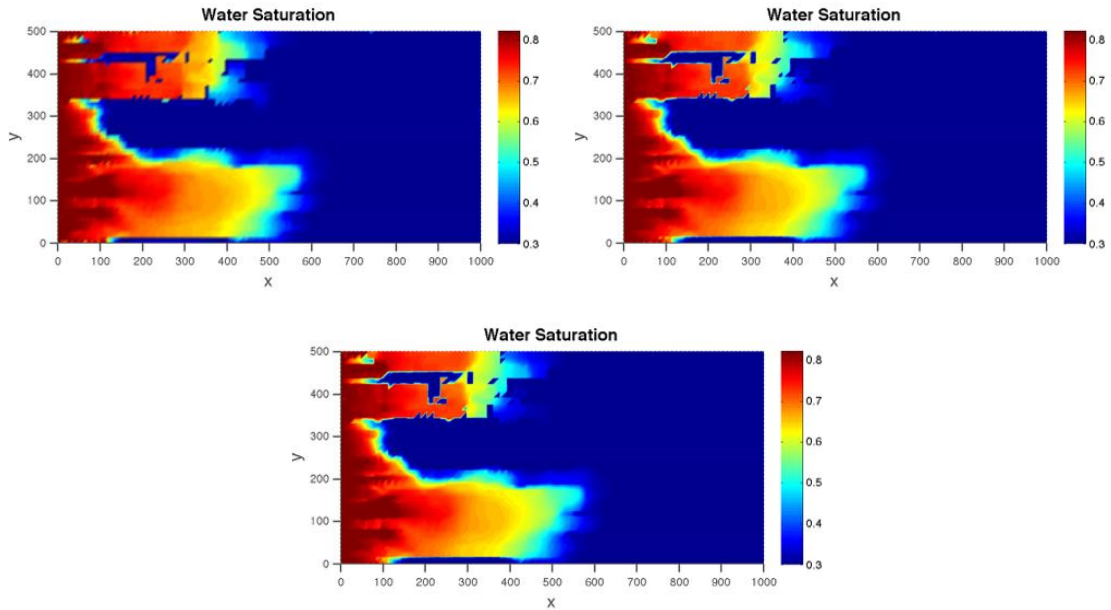


Figure 15: The two-dimensional water saturation contours at 65 days for the convergence study example on  $\mathcal{M}_2$  using NIPG with  $p = 1$  (top),  $p = 2$  (middle), and  $p = 3$  (bottom) and  $\sigma = 1.0$ .

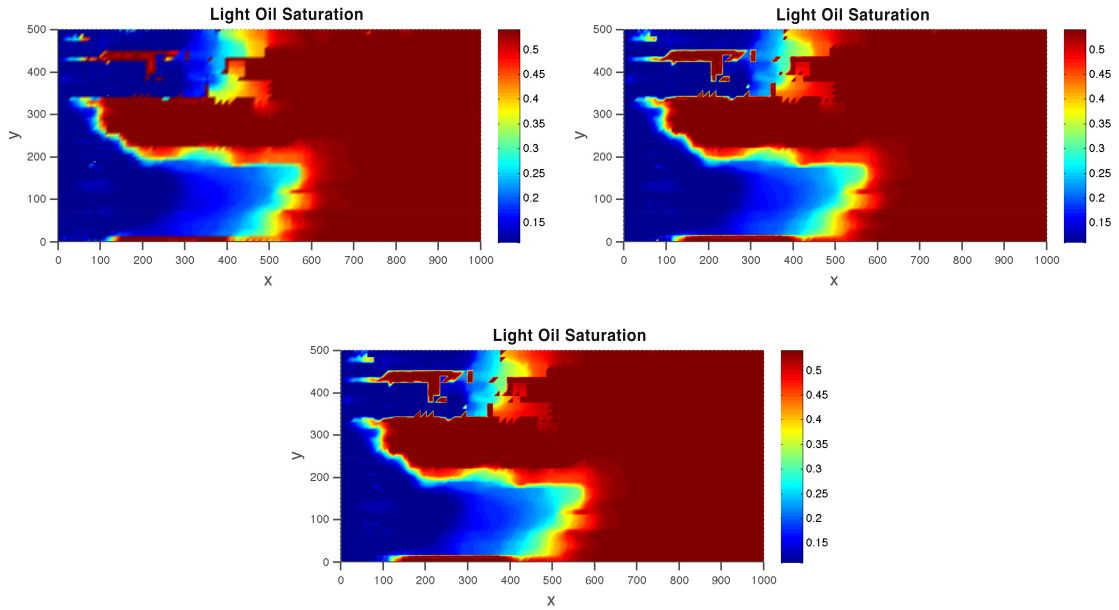


Figure 16: The two-dimensional light oil saturation contours at 65 days for the convergence study example on  $\mathcal{M}_2$  using NIPG with  $p = 1$  (top),  $p = 2$  (middle), and  $p = 3$  (bottom) and  $\sigma = 1.0$ .

The final time is  $t_s = 65.0$  days. The mass loss at each time step is given in Figure 19 for piecewise linear and quadratic solutions.

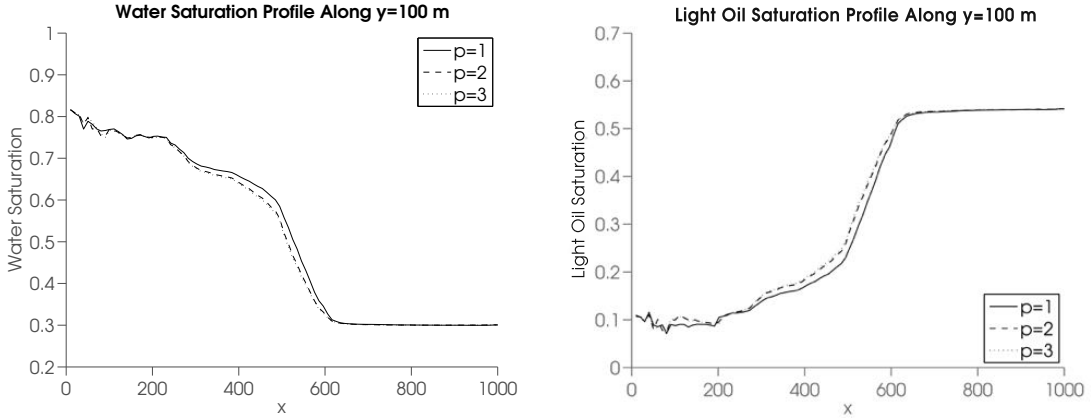


Figure 17: The one-dimensional saturation contours at 65 days for the convergence study example on  $\mathcal{M}_2$  using NIPG with  $p = 1$  (solid line),  $p = 2$  (dashed line), and  $p = 3$  (dotted line) and  $\sigma = 1.0$ .

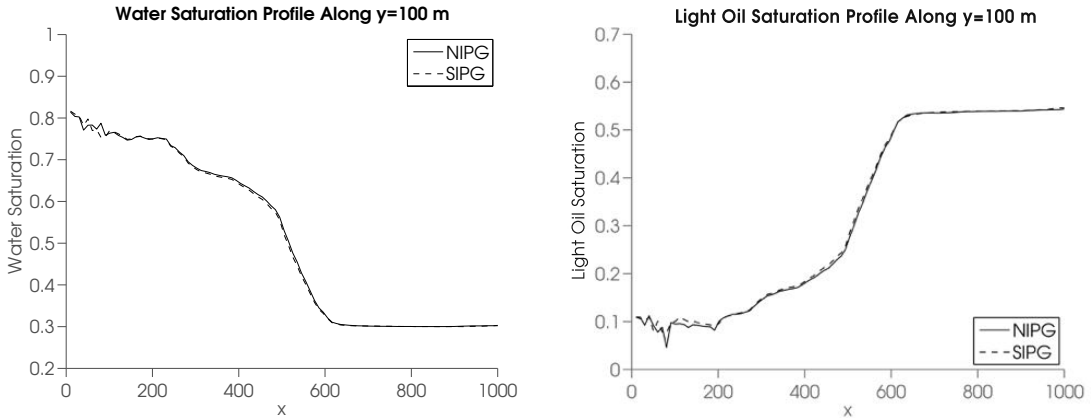


Figure 18: The one-dimensional saturation contours at 65 days for the convergence study example on  $\mathcal{M}_2$  using NIPG (solid line) and SIPG (dashed line) with  $p = 2$  and  $\sigma = 1.0$ .

We see that the mass loss is small as we expect of the DG scheme: it is of the order of  $10^{-5}$  for the water and light oil saturations, and of the order of  $10^{-7}$  for the oil saturation. The maximum mass loss for each phase over all mesh elements and time steps is given in Table 1.

	$p = 1$	$p = 2$
$\max_k \max_T E_{s_o,T}^k$	$4.4698 \times 10^{-7}$	$9.4353 \times 10^{-7}$
$\max_k \max_T E_{s_w,T}^k$	$5.2374 \times 10^{-5}$	$6.2000 \times 10^{-5}$
$\max_k \max_T E_{s_g,T}^k$	$8.9670 \times 10^{-5}$	$7.2000 \times 10^{-5}$

Table 1: The maximum mass loss over all time steps and mesh elements for the phase saturations after 65 days using NIPG with  $p \in \{1, 2\}$  and  $\sigma = 1.0$ .

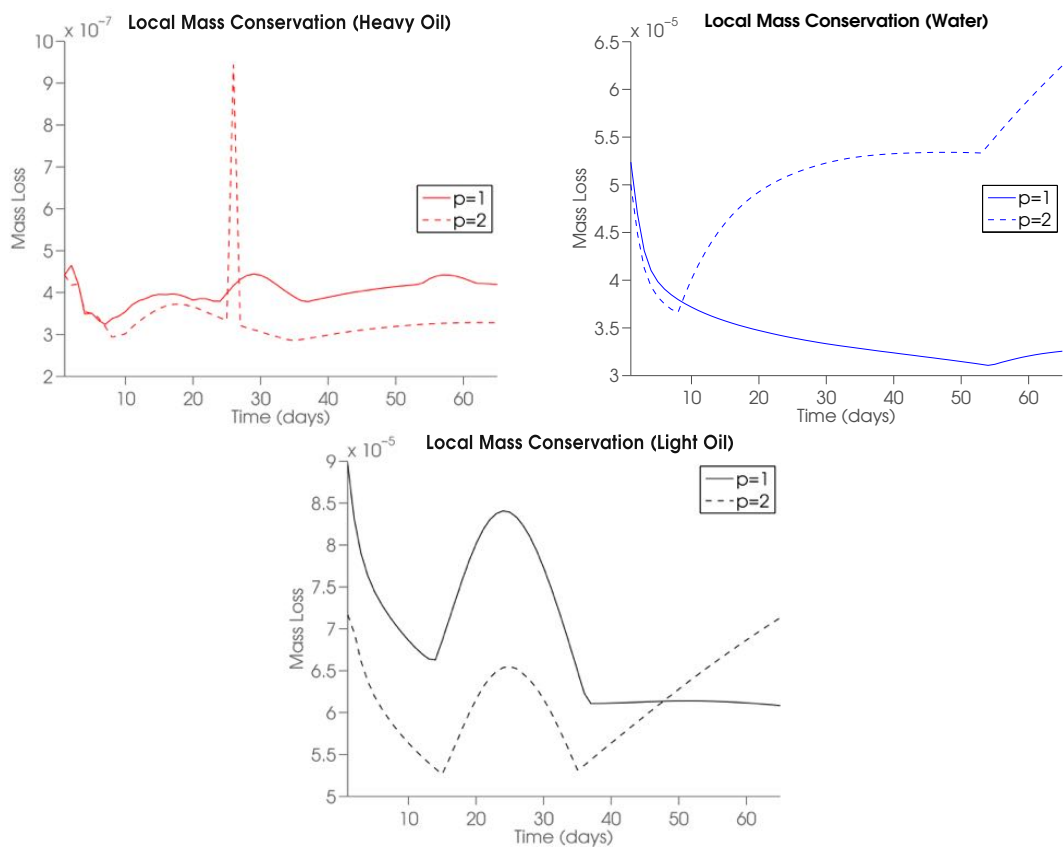


Figure 19: The mass loss for the heavy oil, water, and light oil saturations for the SPE 10 benchmark problem using  $p \in \{1, 2\}$  and  $\Delta t = 1.0$  day.

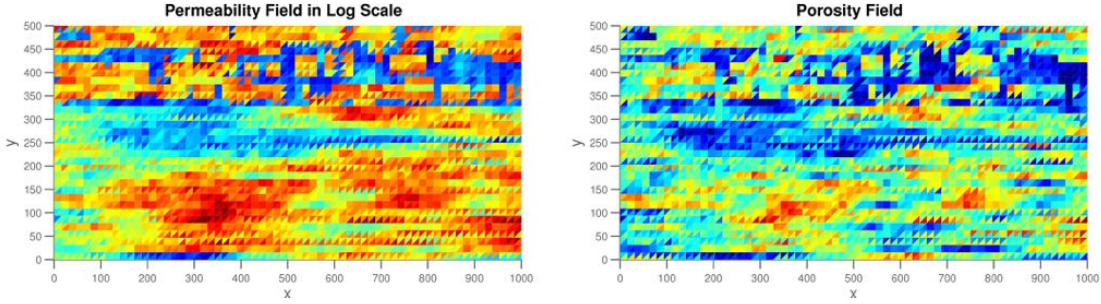


Figure 20: The permeability field and porosity field for the first SPE 10 benchmark example.

## 5.5 Heterogeneous porosity and permeability

Next, we test the scheme using input data from the SPE 10 benchmark problem [11]. Namely, we consider two-dimensional slices of the provided three-dimensional permeability and porosity fields. There are regions in the domain for which the porosity degenerates.

For the first test, we take a  $120 \times 54$  cell cut of the 30th vertical layer of the permeability field and porosity field. A visualization of the permeability and porosity fields is given in Figure 20. The upper portion of this field represents a Tarbert formation while the lower portion represents a fluvial Upper Ness region. The Tarbert formation has more discontinuous geological features than Upper Ness. The porosity field is also piecewise discontinuous and varies from 0 to 46.7%. We consider the computational domain  $\Omega = [0 \text{ m}, 1000 \text{ m}] \times [0 \text{ m}, 500 \text{ m}]$  and partition the domain into a uniform mesh of 16,384 triangular elements. We point out that the porosity is zero for 208 triangles. We use the NIPG method with  $\sigma = 1.0$  and  $p = 3$ . A time step of  $\Delta t = 0.1$  days is used.

The two-dimensional pressure and saturation contours after 102 days are given in Figure 21. We see that the scheme is able to accurately capture a highly varying permeability field across six orders of magnitude. The saturation contours clearly show the phase displacement is more homogeneous in the bottom region than in Tarbet formation. Newton's method converges in 3 to 5 iterations with a tolerance of  $10^{-11}$ . We find that using a sequential semi-implicit solution method allows us to take relatively large time steps while still maintaining stability.

For the second test, we take a  $220 \times 60$  cell cut of the 45th horizontal layer of the permeability and porosity fields. That layer exhibits different geological features than the one for the first test. The domain contains trends, i.e. regions with larger permeability and porosity values, which can be associated to fracture-like features. Visualizations of the permeability and porosity fields are given in Figure 22. The porosity field is also piecewise discontinuous and varies from 0 to 40%.

We again consider the computational domain  $\Omega = [0 \text{ m}, 1000 \text{ m}] \times [0 \text{ m}, 500 \text{ m}]$  and partition the domain into a uniform mesh of 16,384 triangular elements. For this test case, 640 elements have zero porosity and they are grouped together in the geological features. We use the NIPG method with  $\sigma = 1.0$  and  $p = 2$ . A time step of  $\Delta t = 0.1$  days is used. The number of Newton iterations for convergence is initially equal to 6, and then it decreases to 3. The two-dimensional pressure and saturation contours after 150 days are given in Figure 23.

These numerical results show robustness of the semi-implicit scheme of second and third order, for highly varying permeability and porosity fields. Because of the discontinuous approximations, the numerical method easily handles degenerate porosity fields.

## 6 Conclusions

In this work we show the potential of using polynomial approximation of degree up to four for solving an incompressible three-phase flow problem in heterogeneous media. We observe that (i) the

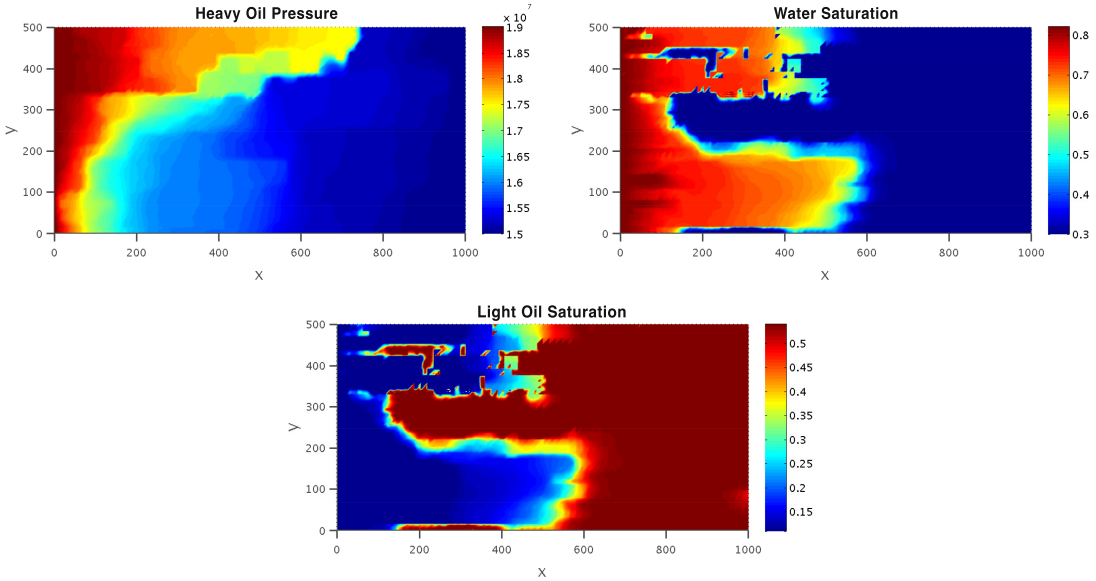


Figure 21: The two-dimensional pressure and saturation contours at 102 days for the first SPE 10 example using piecewise cubic approximations.

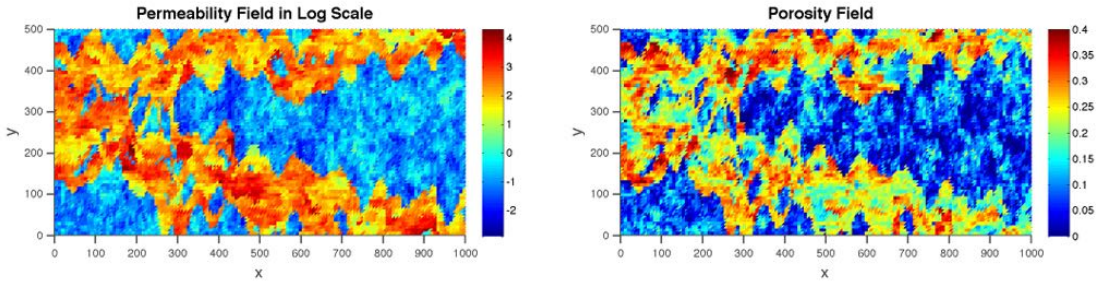


Figure 22: The permeability field and porosity field for the second SPE 10 benchmark example.

numerical mass errors are negligible; (ii) the semi-implicit algorithm stabilizes the solution enough that no slope limiters are required; and (iii) the method converges as the polynomial degree increases even for cases of highly varying discontinuous permeability and porosity fields. In a future work, we would investigate the black-oil problem, which is a three-phase flow with mass transfer between the phases.

## References

- [1] Abreu, E., Douglas, J., Furtado, F., Marchesin, D., Pereira, F.: Three-phase immiscible displacement in heterogeneous petroleum reservoirs. *Mathematics and computers in simulation* **73**(1), 2–20 (2006)
- [2] Aziz, K., Settari, A.: *Petroleum Reservoir Simulation*. Applied Science Publishers (1979)
- [3] Baker, L.: Three-phase relative permeability correlations. *Society of Petroleum Engineers* (1988). SPE-17369-M

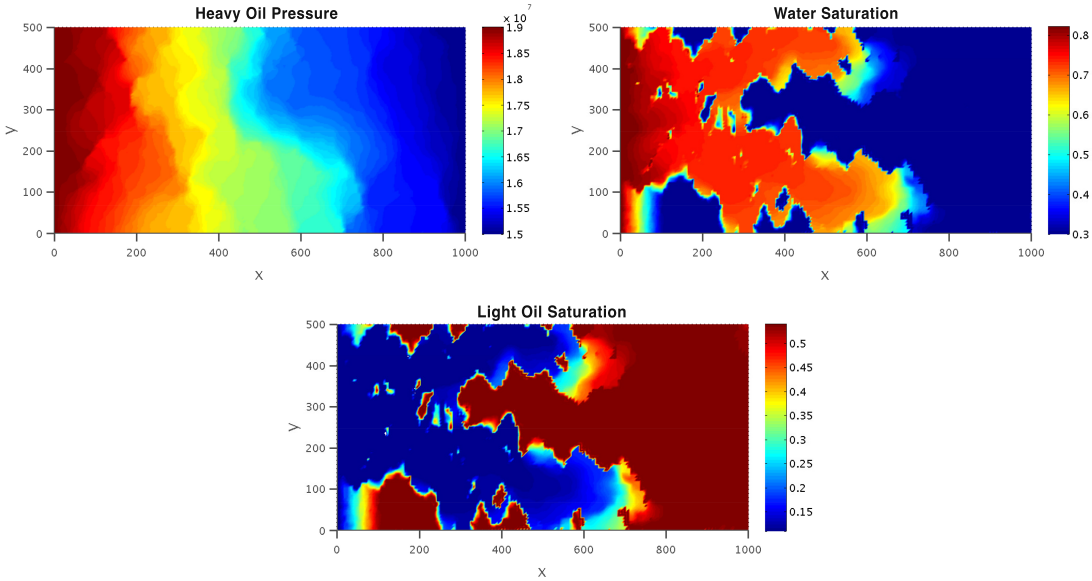


Figure 23: The two-dimensional pressure and saturation contours at 150 days for the second SPE 10 example using piecewise quadratic approximations.

- [4] Bastian, P.: A fully-coupled discontinuous Galerkin method for two-phase flow in porous media with discontinuous capillary pressure. *Computational Geoscience* **18**, 779–796 (2014)
- [5] Bastian, P., Lang, S.: Complex benchmark computations obtained with the software toolbox ug. *Computational Geosciences* **8**(2), 125–147 (2004)
- [6] Bentsen, R.G., Anli, J.: A new displacement capillary pressure model. *Journal of Canadian Petroleum Technology* **15**(3), 75–79 (1976)
- [7] Berre, I., Dahle, H., Karlson, K., Nordhaug, H.: A streamline front tracking method for two- and three-phase flow including capillary forces. *Proceedings of an AMS-IMS-SIAM, Joint Summer Research Conference on Fluid Flow and Transport in Porous Media: Mathematical and Numerical Treatment* **295**, 49–61 (2002)
- [8] Brooks, R., Corey, A.: Hydraulic properties of porous media. *Hydrol. Pap.* **3** (1964)
- [9] Chen, Z., Ewing, R.E.: Comparison of various formulations of three-phase flow in porous media. *Journal of Computational Physics* **132**(2), 362–373 (1997)
- [10] Chen, Z., Huan, G., Ma, Y.: Computational methods for multiphase flows in porous media. Society for Industrial and Applied Mathematics (SIAM), Philadelphia (2006)
- [11] Christie, M., Blunt, M.: Tenth SPE comparative solution project: a comparison of upscaling techniques. *SPE Reservoir Engineering and Evaluation* **4**, 308–317 (2001)
- [12] Dong, J.: A high order method for three phase flow in homogeneous porous media. *SIAM Undergraduate Research Online* **7** (2014)
- [13] Epshteyn, Y., Riviere, B.: Fully implicit discontinuous finite element methods for two-phase flow. *Applied Numerical Mathematics* **57**, 383–401 (2007)

- [14] Ern, A., Mozolevski, I.: Discontinuous Galerkin method for two-component liquid gas porous media flows. *Computational Geosciences* **16**, 677–690 (2012)
- [15] Ern, A., Mozolevski, I., Schuh, L.: Discontinuous Galerkin approximation of two-phase flows in heterogeneous porous media with discontinuous capillary pressures. *Computer Methods in Applied Mechanics and Engineering* **199**, 1491–1501 (2010)
- [16] Klieber, W., Rivière, B.: Adaptive simulations of two-phase flow by discontinuous galerkin methods. *Computer methods in applied mechanics and engineering* **196**(1), 404–419 (2006)
- [17] Li, J., Riviere, B.: Numerical solutions of the incompressible miscible displacement equations in heterogeneous media. *Computer Methods in Applied Mechanics and Engineering* (to appear)
- [18] Lu, Q., Peszynska, M., Wheeler, M.: A parallel multi-block black-oil model in multi-model implementation. *Society of Petroleum Engineers* **7**, 278–287 (2002). SPE 79535
- [19] Natvig, J.R., Lie, K.A.: Fast computation of multiphase flow in porous media by implicit discontinuous galerkin schemes with optimal ordering of elements. *Journal of Computational Physics* **227**(24), 10,108–10,124 (2008)
- [20] Rankin, R., Riviere, B.: A high order method for solving the black-oil problem in porous media. *Advances in Water Resources* (to appear)
- [21] Trangenstein, J.A., Bell, J.B.: Mathematical structure of the black-oil model for petroleum reservoir simulation. *SIAM Journal on Applied Mathematics* **49**(3), 749–789 (1989)